THE JOURNAL OF PHYSICAL CHEMISTRY C

C: Plasmonics; Optical, Magnetic, and Hybrid Materials

Lasing Conditions of Transverse Electromagnetic Modes in Metallic-Coated Micro- and Nanotubes

Nicolás Passarelli, Raúl Alberto Bustos-Marún, and Ricardo A Depine

J. Phys. Chem. C, **Just Accepted Manuscript** • DOI: 10.1021/acs.jpcc.9b01808 • Publication Date (Web): 23 Apr 2019

Lasing Conditions of Transverse Electromagnetic Modes in Metallic-Coated Micro- and Nanotubes

Nicolás Passarelli,[†] Raúl Bustos-Marún,[*,†] and Ricardo Depine[‡]

[†]*Instituto de Física Enrique Gaviola (IFEG-CONICET) and Facultad de Ciencias Químicas, Universidad Nacional de Córdoba, Ciudad Universitaria, Córdoba 5000, Argentina*

[‡]*Grupo de Electromagnetismo Aplicado, Departamento de Física, FCEN, Universidad de Buenos Aires and IFIBA, Consejo Nacional de Investigaciones Científicas y Técnicas (CONICET), Ciudad Universitaria, Pabellón I, C1428EHA, Buenos Aires, Argentina*

E-mail: rbustos@famaf.unc.edu.ar

Abstract

In this work, we study the lasing conditions of the transverse electric modes (TE) of micro- and nanotubes coated internally with a thin metallic layer. This geometry may tackle some of the problems of nanolasers and spasers as it allows the recycling of the active medium while providing a tunable plasmonic cavity. The system presents two types of TE modes: cavity modes (CMs) and whispering-gallery modes (WGMs). On the one hand, we show that the lasing of WGM is only possible in nanoscale tubes. On the other hand, for tubes of some micrometers of diameter, we found that the system presents a large number of CMs with lasing frequencies within the visible and near-infrared spectrum and very low gain thresholds. Moreover, the lasing frequencies of CMs can be accurately described by a simple one-parameter model. Our results may be useful in the design of micro- and nanolasers for "lab-on-chip" devices, ultra-dense data storage, nanolithography, or sensing.

INTRODUCTION

Micro- and Nanolasers (lasers of micro- or nanoscale dimensions)[1–3] and spasers (a type of laser which confines light at subwavelength scales by exciting surface plasmon polaritons)[4,5] can be used to provide a controllable source of "on-demand" electromagnetic fields at very small size scales.[6] These devices can find numerous applications for enhanced spectroscopies, as a way of counteracting the effect of optical losses in different plasmonic devices, or directly as a source of radiation for "lab-on-chip" devices, ultra-dense data storage, or nanolithography.[7–11] Different forms of nanolasers and spasers have been extensively discussed in the literature over the last decades, both from the theoretical[5,11–17] and the experimental[1–3,11,18–25] point of view. There has been studied a wide variety of structures

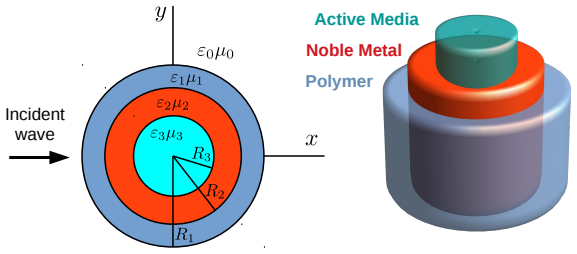

Figure 1: Scheme of the system treated. An infinite multiwall cylinder where the core allows the circulation of a solution with the dye (active medium), the intermediate wall provides the plasmonic cavity, and the outer wall gives the physical support to the system. The "incident wave" is just used to numerically find the poles of the scattering cross-section. See text for more details.

and materials/metamaterials for supporting the spaser/nanolaser as well as different compounds to act as the optical-gain medium. This includes cavities in thin films, different forms of waveguides made of lithographic or nanoprinted surfaces, graphene sheets, carbon nanotubes, nanoparticle or quantum dot arrangements, etc.[4,6]

There are, in general, two main problems involved in the design of spasers and nanolasers. One is the need for a good matching between the plasmonic resonances (for spasers) or the cavity resonaces (for nanolasers) and the emission cross-section of the active medium. The other main problem is photobleaching, or the irreversible photo-degradation of the molecules[26] or quantum dots[21] that form the active media. Other features are also desirable, such as large volumes of hot-spots,[27] to allow the study of large molecules, or the presence of several resonances that can be used for lasing with different active media.[25] The ideal design of a nanolaser or a spaser should not only solve the photobleaching problem but should also offer some flexibility to finely tune the frequencies of resonances[24,25,28] while providing large volumes of hot-spots and low gain thresholds.

In this work, we study the lasing conditions of a geometry that seems promising to meet all the above requirements. The proposed geometry, see Fig. 1, allows the recycling of the active medium (thanks to microfluidics[23]), provides a tunable resonant cavity (by modifying the dielectric constant of the solution of the core, physically separates the active medium from the external medium (where analytes may be placed for instance), presents large volumes of hot-spots, low gain threshold, and a large number of resonances within the visible and near-infrared spectrum.

The work is organized as follow. In section "General remarks", we discuss some generalities of the studied system. In section "Scattering Problem", we explain how to solve the scattering problem in the linear-response regime. There, we give the equations of the electromagnetic fields in terms of cylindrical harmonics, the boundary conditions, the expressions for the cross-sections, and the relation between the scattering cross-sections and the near fields at the lasing condition. In section "Modeling the optical active medium", we discuss the different approximations used to describe the active medium and how we obtained the parameters of the dyes used. In section "Lasing conditions", we discuss the lasing conditions in terms of lasing frequencies and gain thresholds, providing also some approximations for their estimation. In section "Results", we show the main results of the work and summarize them in the "conclusions" section.

THEORY

General remarks. The theoretical treatment of the system is sustained in two major axes. The first one is an extension of well known analytical solution of an infinite two-wall concentric cylinder[29–32] to three-wall concentric cylinders, including the expressions for the scattering and extinction cross-sections. The second axis is the modeling of the active medium. We use two different models: a wideband approach, which neglects the frequency dependence of the active medium, and a Lorentz-like model for the frequency dependence of the active medium.

Although we performed several calculations with different geometries, most of the work is focused on one representative example. This

geometry consists of three concentric cylinders, see Fig. 1. The internal core of 2000nm of radius consists of a dielectric solvent and a dissolved dye. The inner wall of the tube is a layer of 25 nm of a plasmonic material (gold), and the outer one, of 475 nm, is a dielectric (polymer) that provides mechanical support to the cavity and separates it from the external medium.

Due to its sizes, the system lays between the microlaser and nanolaser categories. Furthermore, due to the metallic coating, the lasing of some resonances turn the system into a spaser. For simplicity, throughout this paper we will use the generic term nanolaser to refer to the system, but keeping in mind these considerations.

The geometry was inspired by recent works that present polymer microtubes suitable for fluidics[21,33–36] The fact that the system allows the circulation of a fluid through it, can be used for recycling the active media as well as to deposit the metal layer by chemical methods.[37–39] The recycling of the active media may help to counteract the photobleaching of the dye molecules acting as the optically active medium. The intermediate layer provides the plasmonic cavity that will control the resonance frequencies and the outer layer gives the physical support to the system. In this way, if for example the nanolaser is used for sensing purposes, the analyte is physically separated from the active medium. The latter not only avoids undesired chemical interferences but can also be used to control the resonances of the nanolaser by tunning the dielectric constant of the inner cylinder.

Similar geometries have been studied before, including wires, tubes, pores, as well as fibers or capillaries.[21,36,40–43] The sizes of these systems ranged from tens of nanometers up to hundreds of micrometers of radius. The geometries within the nanometers scale have been studied theoretically for perpendicular illumination, which excites the TE modes of lasing, but generally within quasi-static approximations. The larger geometries have been studied mainly in the context of low loss communication, where the longitudinal modes of lasing are the "important" ones.[44–50] The resonances in such a case can be thought as Fabry-Pérot modes[51] for finite systems, or they can be treated as dispersion relations for infinite cylinders.[52]

Regarding the feasibility of the proposed geometry, modern techniques of fabrication show that tubes of some few microns, suitable for microfluidics, can be produced[53–57] and it is even possible to make them of different materials.[33,34,58–60] On the other hand, coating of surfaces with very thin layers of noble metals has been employed in several experimental works using different techniques.[61,62]

The incident wave, shown in Fig. 1, is used in the calculations to find the poles of the scattering cross-section of the system, which leads us to the lasing conditions. We will only consider the case of electric fields perpendicular to the z axis of the cylinders, as we are studying non-magnetic materials. For this polarization, the resonances will be found when the perpendicular component of the incident wave matches the resonant condition, and this is why we need only to consider the perpendicular incidence.

The dielectric constant of gold as a function of the wavelength was taken from Ref.[63] The dielectric constant of the polymer was considered constant with $\varepsilon_1 = 2.22$.[64] The theoretical treatment of the dielectric constant of the active medium is discussed in details in section "Modeling the optical active medium".

Scattering problem. The analytical solution for the scattering of electromagnetic plane waves incident perpendicularly on a homogeneous circular cylinder of infinite length is well known.[31] In this case, and due to the translational invariance of the geometry, the solution of the rigorous electromagnetic vectorial problem can be reduced to the treatment of two independent scalar problems, corresponding to the following two basic polarization modes in which the polarization of the interior and scattered fields maintain the polarization of the incident wave: i) s (or TM) polarization, when the incident electric field is directed along the cylinder axis, and ii) p (or TE) polarization, when the incident magnetic field is directed along the cylinder axis In the first case, it is clear that the electric field can only induce electric currents directed along the cylinder axis but

not along the azimuthal direction, thus preventing the existence of localized surface plasmons in metallic cylinders for s (or TM) polarization. For p polarization, on the other hand, the electric field, contained in the main section of the cylinder, can induce azimuthal electric currents which, under appropriate conditions, give place to localized surface plasmon resonances.

For multilayered cylinders with an arbitrary number of layers,[29,30,65] similar conclusions can be obtained: the solution of the rigorous electromagnetic vectorial problem can be separated into two independent (s and p) scalar polarization modes and, when metallic layers are involved, localized surface plasmon resonances occur for p, but not for s, incident polarizations. Taking into account that we are interested in the TE modes of nanolasers, in what follows we restrict our attention just to the case of p polarization.

To model the linear response of our system we consider an infinitely long circular cylinder (the core) covered with two concentric layers of homogeneous materials and illuminated from a semi-infinite ambient medium. We assume that all the materials involved are isotropic and linear and characterized by a dielectric constant ε_j and a magnetic permeability μ_j ,$(j = 0, 1, 2, 3)$, where $j = 0$ corresponds to the ambient and $j = 3$ corresponds to the core (see figure 1). The Gaussian system of units is used and an $\exp(+i\omega t)$ time-dependence is implicit throughout the paper, with ω the angular frequency, c the speed of light in vacuum, t the time, and $i = \sqrt{-1}$.

Fields representation. Using polar coordinates (r, θ), where θ is the angle respect to the x axis of a vector contained in the $x - y$ plane of modulus r, all the fields in the p polarization case can be written in terms of $F_j(r, \theta)$, the non-zero component of the total magnetic field along the axis of the cylinder and evaluated in region j. According to Maxwell's equations, $F_j(r, \theta)$ must satisfy Helmholtz equations in each region

$$(\nabla^2 + k_j^2) F_j = 0\,, \tag{1}$$

with $k_j = \omega m_j / c$ and $m_j = (\varepsilon_j\, \mu_j)^{1/2}$ the refractive index of medium j. Following the usual separation of variables approach, $F_j(r, \theta)$ can be represented with the following multipole expansions

$$F_j(r, \theta) = \sum_{n=-\infty}^{\infty} \left[a_{jn} J_n + A_{jn}\, H_n\right] \mathrm{e}^{in\theta} \tag{2}$$

where a_{jn}, A_{jn} $(j = 0, \ldots 3)$, are complex amplitudes, $J_n(k_j r)$ is the n-th Bessel function of the first kind and $H_n(k_j r)$ is the n-th Hankel function of the second kind, with asymptotic behavior for large argument $(|x| \to \infty)$

$$H_n(x) \longrightarrow \sqrt{\frac{2}{\pi x}}\, \mathrm{e}^{\,-i(x - n\pi/2 - \pi/4)}\,. \tag{3}$$

The amplitudes a_{0n} in the medium of incidence are determined by the incident wave. Assuming, without loss of generality, a unit-amplitude incident plane wave propagating along the x-axis, and using the Jacobi-Anger expansion.[66]

$$\mathrm{e}^{-ik_0 r \cos\theta} = \sum_{n=-\infty}^{\infty} (-i)^n J_n(k_0 r)\, \mathrm{e}^{in\theta} \tag{4}$$

the amplitudes a_{0n} are given by

$$a_{0n} = (-i)^n\,. \tag{5}$$

For physical reasons, Hankel functions of the second kind, singular at the origin, are not allowed in the field representation of the core region. Thus

$$A_{3n} = 0. \tag{6}$$

Therefore, in order to evaluate the magnetic field $\vec{H}_j = F_j\, \hat{z}$ everywhere with expansions (2), a sextuple infinity of unknown amplitudes, namely, $A_{0n}, a_{1n}, A_{1n}, a_{2n}, A_{2n}, a_{3n}$, must be found. Finally, the electric field $\vec{E}_j$ in p polarization in terms of $F_j(r, \theta)$ can be obtained from Ampère's Law

$$\nabla \times (F_j\, \hat{z}) = i\, \frac{\omega}{c} \varepsilon_j\, \vec{E}_j\,. \tag{7}$$

Boundary conditions. At the boundary $r = R_j$ $(j = 1, \ldots 3)$ between two homogeneous regions, the continuity of the tangential components of the electric and magnetic field

must be fulfilled and these conditions are equivalent to the continuity of F_j and $\frac{1}{\varepsilon_j}\frac{\partial F_j}{\partial r}$. These boundary conditions provide a system of six linear equations for the six unknown amplitudes $A_{0n}, a_{1n}, A_{1n}, a_{2n}, A_{2n}$ and a_{3n}. Due to the rotational symmetry of the system, the boundary conditions do not couple amplitudes with different multipole order n. The continuity of the z component of the magnetic field gives equations

$$a_{3n}J_n(k_3R_3) = a_{2n}J_n(k_2R_3) + A_{2n}\,H_n(k_2R_3) \tag{8}$$
$$a_{2n}J_n(k_2R_2) + A_{2n}\,H_n(k_2R_2) = a_{1n}J_n(k_1R_2) + A_{1n}\,H_n(k_1R_2) \tag{9}$$
$$a_{1n}J_n(k_1R_1) + A_{1n}\,H_n(k_1R_1) = (-i)^n J_n(k_0R_1) + A_{0n}\,H_n(k_0R_1) \tag{10}$$

whereas the continuity of the tangential component of the electric field gives the equations

$$\frac{k_3}{\varepsilon_3}a_{3n}J_n'(k_3R_3) = \frac{k_2}{\varepsilon_2}[\,a_{2n}J_n'(k_2R_3) + A_{2n}\,H_n'(k_2R_3)\,] \tag{11}$$
$$\frac{k_2}{\varepsilon_2}[\,a_{2n}J_n'(k_2R_2) + A_{2n}\,H_n'(k_2R_2)\,] = \frac{k_1}{\varepsilon_1}[\,a_{1n}J_n'(k_1R_2) + A_{1n}\,H_n'(k_1R_2)\,] \tag{12}$$
$$\frac{k_1}{\varepsilon_1}[\,a_{1n}J_n'(k_1R_1) + A_{1n}\,H_n'(k_1R_1)\,] = \frac{k_0}{\varepsilon_0}[\,(-i)^n J_n'(k_0R_1) + A_{0n}\,H_n'(k_0R_1)\,] \tag{13}$$

where primes denote derivatives of the Bessel and Hankel functions with respect to their arguments. The above equations can be written in matrix form

$$\mathbb{M}\vec{\mathbb{X}} = \vec{\mathbb{B}} \tag{14}$$

with $\vec{\mathbb{X}} = [A_{0n}, a_{1n}, A_{1n}, a_{2n}, A_{2n}, a_{3n}]^T$, $\vec{\mathbb{B}} = (-i)^n\left[J_n(k_0R_1), \frac{k_0}{\varepsilon_0}J_n'(k_0R_1), 0, 0, 0, 0\right]^T$ and

$$\mathbb{M} = \begin{bmatrix} -H_n(k_0R_1) & J_n(k_1R_1) & H_n(k_1R_1) & 0 & 0 & 0 \\ -\frac{k_0}{\varepsilon_0}H_n'(k_0R_1) & \frac{k_1}{\varepsilon_1}J_n'(k_1R_1) & \frac{k_1}{\varepsilon_1}H_n(k_1R_1) & 0 & 0 & 0 \\ 0 & J_n(k_1R_2) & H_n(k_1R_2) & -J_n(k_2R_2) & -H_n(k_2R_2) & 0 \\ 0 & \frac{k_1}{\varepsilon_1}J_n'(k_1R_2) & \frac{k_1}{\varepsilon_1}H_n'(k_1R_2) & -\frac{k_2}{\varepsilon_2}J_n'(k_2R_2) & -\frac{k_2}{\varepsilon_2}H_n'(k_2R_2) & 0 \\ 0 & 0 & 0 & J_n(k_2R_3) & H_n(k_2R_3) & -J_n(k_3R_3) \\ 0 & 0 & 0 & \frac{k_2}{\varepsilon_2}J_n'(k_2R_3) & \frac{k_2}{\varepsilon_2}H_n'(k_2R_3) & -\frac{k_3}{\varepsilon_3}J_n(k_3R_3) \end{bmatrix}$$

Far fields, near fields, and the lasing thresholds. The coefficients A_{0n} determines the amplitude of the scattered wave and can be used to calculate the cross-sections per unit length of the cylinder:

$$C_{sca} = \frac{4\varepsilon_0^2}{k_0}\sum_{n=-\infty}^{\infty}|A_{0n}|^2 \tag{15}$$

$$C_{ext} = \frac{4}{\varepsilon_0^2 k_0}\sum_{n=-\infty}^{\infty}\mathrm{Re}\{A_{0n}\} \tag{16}$$

where C_{sca} and C_{ext} are the scattering and extinction cross-sections respectively.

The poles of C_{sca} and C_{ext} for each order n, can be found as the points in the parameter's space where the determinant of the matrix $\mathbb{M}$ in Eq. 14 cancels. There, the fields associated with a given order n diverge. This condition corresponds to resonances with compensated optical losses and they are identified with the lasing threshold.

As we have already reported for spheres,[67] there is a proportionality relation between the

near and far field at the lasing condition. This can readily be understood by considering the following reasonings. When the determinant of $\mathbb{M}$ approaches zero, all the coefficients of modes n and $-n$ goes to infinity as $\vec{\mathbb{X}} = \mathbb{M}^{-1}\vec{\mathbb{B}}$. Let us recall that as $j_{-n} = (-1)^n j_n$ and $H_{-n} = (-1)^n H_n$, the coefficients $a_{j,n}$ and $a_{j,-n}$ should be equal. Then, at the lasing condition the summation in Eq. 2 can be replaced by the summation of only two terms F_n and F_{-n} (or F_0 for $n = 0$). The same can be done to the cross-sections C_{sca} and C_{ext}, and the electric fields $\vec{E}_j$.

According to Eq. 7 the component of the electric field E can be written in term of the F function as

$$E_r = \frac{-inF}{r} \quad E_\theta = -\frac{\partial F}{\partial r}. \tag{17}$$

Then, $\left|\vec{E}_{0n}\right|^2$, the square modulus of the scattered electric field, at the lasing condition of modes n and $-n$, results in:

$$\left|\vec{E}_{0n}\right|^2 = |A_{0n}|^2 \left|\vec{M}_n\right|^2 \tag{18}$$

where

$$\begin{aligned}\left|\vec{M}_n\right|^2 &= k_0^2\left(|H_{n-1}|^2 + |H_{n+1}|^2\right) \\ &\times \begin{cases} 2\cos^2(n\theta) & n \text{ even} \\ 2\sin^2(n\theta) & n \text{ odd} \\ \frac{1}{2} & n = 0 \end{cases}\end{aligned}$$

We have used above the recurrent relations of the Bessel's and Hankel's functions, $2\partial_x Z_n(x) = Z_{n+1} + Z_{n-1}$ and $(2n/x)Z_n(x) = Z_{n-1} - Z_{n+1}$, where Z_n is J_n or H_n.

Comparing Eqs. 15 and 18 gives the relation between E_0 and C_{sca}.

$$\left|\vec{E}_{0n}\right|^2 = \frac{k}{4\varepsilon^2} C_{sca} \left|\vec{M}_n\right|^2 \tag{19}$$

Note that, as the fields in different regions are connected due to the continuity condition, when the fields in the region 0 goes to infinity the same should happen in every region. Then, the lasing thresholds can be found as zeros of the determinant of Eq. 14, divergences of C_{sca}, or divergences of the electric/magnetic fields in an arbitrary position. In principle, the last two strategies could be cumbersome because of dark modes or the presence of nodes in the harmonics respectively. However, dark modes can be problematics only for modes with A_{0n} strictly zero. In our case, even modes with values of A_{0n} really small, which can safely be marked as dark modes as A_{0n} is orders of magnitude smaller than the average value per mode, show divergences of C_{sca} easily found numerically. For example, in the upper panel of Fig. 9 one can check that even poles with A_{0n} almost zero, just over the y-axis of the figure, can be found numerically as divergences of C_{sca}.

Modeling the optical active medium The solution of the scattering problem discussed in the previous sections requires the value of the complex dielectric constant $\varepsilon = \varepsilon' + i\varepsilon''$ of each component for the wavelengths of interest. The imaginary part of it reflects the amount of absorption or emission of light. In our treatment and due to the temporary dependence used, ε'' has a positive sign for an active medium and a negative sign for an absorbing medium. The Clausius-Mossotti relation determines the dielectric constant of a mixture of molecules in terms of the number of molecules of each type per unit of volume N_i and with molecular polarizability α_i:

$$\frac{\varepsilon - 1}{\varepsilon + 2} = \sum_i \left(4\pi \frac{N_i \alpha_i(\omega)}{3}\right) \tag{20}$$

Considering a diluted solution of an excited dye (subscript dye) dissolved in a non-absorbing host medium (subscript h), the first order Taylor expansion in N_{dye}/N_h leads to:

$$\varepsilon \approx \varepsilon_h + \left(\frac{2 + \varepsilon_h}{3}\right)^2 4\pi N_{dye}\alpha_{dye}(\omega) \tag{21}$$

One can take a simple two-level system for modeling the polarizability of the dye,[68] which, assuming a complete population inversion of the

dye and the sign convention for ε'', results in

$$\alpha(\omega) = \frac{\left(\frac{|\mu_{12}|^2}{\hbar}\right)\left(\omega_0 - \omega + i\frac{\gamma}{2}\right)}{(\omega_0-\omega)^2 + \left(\frac{\gamma}{2}\right)^2\left(1 + 2\left(\frac{\omega_R}{\gamma}\right)^2\right)} \tag{22}$$

where $\vec{\mu}_{12}$ is the transition dipole moment between the ground and excited states with an energy difference of $\Delta E = \hbar\omega_0$, γ is a phenomenological damping term, and $\omega_R = \left|\vec{\mu}_{e\to g}\cdot\vec{E}\right|/\hbar$ is the Rabi frequency. As can be noticed, Eq. 22 takes into account saturation effects. However, in the present paper we will not take them into account for the following reasons: Given that the electromagnetic fields inside the structures analyzed (with a large radius) is not homogeneous, the inclusion of saturation effects will introduce spatial inhomogeneities into the dielectric constant of the active medium. This will break the symmetry of the problem, making the expansion of the fields in Eq. 2 not very useful, as now additional boundary conditions are required, see section "Boundary conditions". In such a case, the present approach does not offer advantages over other methods such as finite elements for example. As discussed in several references,[67,69] not taking into account saturation effects has the consequence that fields go to infinity once optical losses are compensated. However, this divergences can indeed be used to find the lasing conditions, which is the main point of the present work.

Combining Eq. 21 and Eq. 22 (neglecting saturation effects) results in

$$\varepsilon = \varepsilon_h + \varepsilon_l \frac{(\omega_0 - \omega + i\frac{\gamma}{2})\left(\frac{\gamma}{2}\right)}{(\omega_0-\omega)^2 + (\frac{\gamma}{2})^2}, \tag{23}$$

where ε_l is the maximum value of the imaginary part of the dielectric constant ε''

$$\varepsilon_l = \left[\frac{2+\varepsilon_h}{3}\right]^2\left(\frac{8\pi N_{dye}|\mu_{12}|^2}{\hbar\gamma}\right) \tag{24}$$

Note that, as we are assuming a complete population inversion of the dye, every molecule contributes to the stimulated emission of radiation, thus N_{dye} is directly its concentration.

One additional approximation that is normally used to describe an optical active medium is the wideband approximation, which comes from taking $|\omega - \omega_0| \ll \gamma/2$. In this case Eq. 23 turns into

$$\varepsilon = \varepsilon_h + i\varepsilon_l. \tag{25}$$

It should be mentioned that the wideband approximation does not comply with the Kramers-Kronig relation[31,32,68] nor does it take into account the spectral line of any particular dye. However, at a maximum of absorption or emission, that is to say at the resonant wavelength of the dissolved dye, it happens that the contribution to the imaginary part of the refractive index presents a maximum while the real part goes to zero. Under this condition Eq. 25 becomes exact. The wideband approximation is useful for a first exploration of the system as it allows one to calculate the optical response of a system independently of the characteristic of the active medium. Then, after choosing the poles of C_{sca} to be used, a specific dye can be selected and a better approach can be used.[67]

We used water as the host medium, $\varepsilon_h = 1.77$, Lasing conditionsin most of the calculations except in Fig. 6 where we also use ethanol, $\varepsilon_h = 1.85$. The values of γ and ε_l for the different dyes were adjusted from their emission spectra using the Füchtbauer-Ladenburg method as described in the next section.

Parameters of the dyes. While the spectral shape of fluorescence light is relatively easy to measure, it is much more challenging to measure its absolute values due to the difficulty of measuring accurately some quantities such as doping concentration, the degree of electronic excitation, collection and detection efficiencies, etc. The Füchtbauer-Ladenburg method[70] is used to obtain the absolute scaling of the emission cross-section spectrum. In this method, one exploits the fact that the excited-state lifetime is close to the radiative lifetime τ_{rad}, which itself is determined by the emission cross-section $\sigma(\omega)$ for transitions to any lower-lying energy level. This is quantitatively described

by the equation

$$\frac{1}{\tau_{rad}} \approx \frac{2\varepsilon_h}{\pi c^2}\int \omega^2 \sigma(\omega) d\omega.$$

Knowing the spectral intensity of fluorescence $I(\omega)$, proportional to $\sigma(\omega)$, and using the above equation one finds

$$\sigma(\omega) = \frac{\pi c^2}{2\varepsilon_h \tau_{rad}} \frac{I(\omega)}{\int \omega^2 I(\omega) d\omega} \qquad (26)$$

Typically, the spectra of the dyes $I(\omega)$ are fitted to a Lorentzian function

$$I(\omega) = \frac{(\gamma/2)^2}{(\omega_0 - \omega)^2 + (\gamma/2)^2}.$$

Since typically the width of the emission spectrum γ is much smaller than the position of the resonance ω_0, one can take the ω^2 factor out of the integrand of Eq. 26. This yields

$$\sigma(\omega) = \frac{c^2}{\varepsilon_h \tau_{rad} \omega_0^2 \gamma} I(\omega). \qquad (27)$$

Table 1: Parameters of dyes used in Fig. 3. N_i is the concentration of molecules in the excited state required to obtain $\varepsilon_l = 0.05$. The values of τ_{rad} and the spectra of the dyes, from which we obtained ν_0 and γ, were taken from Ref.[71] The values of μ_{12} are calculated from Eq. 30. Values in the third and fourth columns are in 10^{14}Hz, or in nm between parentheses.

	τ_{rad} (ns)	ν_0	$\gamma/2\pi$	$\lvert\mu_{12}\rvert$ (D)	N_i (μM)
Alexa-fluor-680	1.200	4.27 (702)	0.226 (13265)	6.847	6.781
Oregon-green-488	4.100	6.03 (497)	0.331 (9057)	2.203	0.480
Atto-rho3b	1.500	5.03 (596)	0.336 (8923)	4.786	2.231
Atto-725	0.500	3.96 (757)	0.266 (11270)	11.843	17.262
cy3b	2.800	5.37 (558)	0.375 (7995)	3.171	0.878
tCO	3.000	6.40 (468)	1.248 (2402)	2.358	0.146

On the other hand, the relation between the emission cross-section and the polarizability (in cgs) can be written as[68]

$$\sigma_{aligned}(\omega) = \frac{4\pi\varepsilon_h \omega}{c} \mathrm{Im}[\alpha(\omega)]. \qquad (28)$$

where one is assuming a perfect alignment between the electric field and the molecule. The maximum value of the macroscopic, orientation-averaged, cross-section σ_{max}, can be obtained by inserting Eq. 22 into 28 with $\omega = \omega_0$,

$$\sigma_{max} = \frac{\sigma_{aligned}(\omega_0)}{3} = \frac{8\pi \left|\mu_{12}\right|^2 \varepsilon_h \omega_0}{3\hbar\gamma c}. \qquad (29)$$

Comparing Eqs. 27 and 29 allow us to obtain the value of μ_{12} that fits the experiments,

$$|\mu_{12}| = \left(\frac{c}{\omega_0}\right)^{3/2} \left(\frac{3\hbar}{8\pi\varepsilon_h^2 \tau_{rad}}\right)^{1/2}. \qquad (30)$$

The dyes used in this work, see Fig. 3, were chosen because they are soluble, present high quantum yields, and their fluorescence spectra and radiative lifetimes are easily accessible.[71] Table 1 show the dyes used, the values of τ_{rad} reported by the manufacturer, the values of ν_0 and γ obtained from the fitting of the reported spectra, the values of μ_{12} obtained from Eq. 30, and the concentration required to reach $\varepsilon_l = 0.05$. The value of ε_l used ensures the lasing condition over all the frequency range studied. Note that the calculation of the concentrations of the dyes shown in the table, of the order of μM, assumes a complete population inversion, which may require a very intense pumping laser.

However, even if only 1 out 1000 molecules is in the excited states the concentrations of the dyes require to ensure the lasing conditions are of the order of mM, which does not seem too high considering that all dyes are highly soluble in water.

Lasing conditions Within the interval of parameters explored, see section "Results", the analyzed system presents two types of modes, the cavity and the whispering-gallery modes (CMs and WGMs respectively). The former corresponds to modes where the fields are mostly concentrated within the region of the active media and there is a wave pattern along the radius. The WGMs are modes where the fields are concentrated close to the metal layer and there is a wave pattern along the circumference of the cylinder. Typical near fields of both types of modes are shown in Fig. 2. Note that the lasing of WGMs turns the system into a spaser, where the light is highly confined close to the metal layer due to the excitation of surface plasmon polaritons. On the other hand, and due to the fields distribution, the lasing of CMs turns the system into what can be considered a metallic-coated nanolaser (o microlaser depending on the sizes).[11] Therefore, the proposed system has the peculiarity of being, at the same time, a spaser and a metallic-coated nanolaser, depending on which mode is lasing.

As we will see in section "Results", the cavity modes present far lower gain thresholds, which, due to the large number of poles, makes the whispering-gallery modes unreachable within the visible spectrum, for the main geometry studied. For that reason, we will focus on the lasing conditions of cavity modes.

Lasing frequencies of cavity modes. To find the resonant frequencies of the system we will assume a cavity-like model where the standing wave pattern arises from that of waves confined in a cylindrical cavity. This is justified by the gold layer surrounding the active medium. Under this model and neglecting the imaginary part of k_3, the resonant condition occurs when the argument of the Bessel's function J_n corresponding to region 3 ($k_3 r$) becomes zero at the

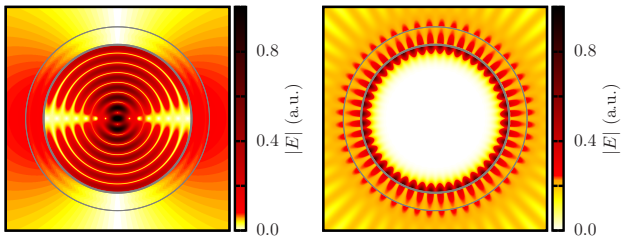

Figure 2: **Left panel -** Near field of a typical cavity mode close to its gain threshold, $\nu = 4.29 \times 10^{14}$Hz $\varepsilon_3'' = 0.0124$. **Right panel -** Near field of a typical whispering-gallery mode close to its gain threshold, $\nu = 4.25 \times 10^{14}$Hz $\varepsilon_3'' = 0.1532$. The geometry is that of Fig. 1 with $R_3 = 2000$nm, $R_2 - R_3 = 25$nm, and $R_1 - R_2 = 475$nm. The electric fields are normalized to their respective maximum values.

boundary between regions 2 and 3, $r = R_3$, i.e.

$$\omega_{n,i} = \frac{c}{m_h R_3} u_{n,i} \tag{31}$$

where $u_{n,i}$ is the i-th non trivial zero of the J_n Bessel's function, we are taking $m_3 \approx m_h$ (m_h is the refractive index of the host of the active medium), R_3 is defined in Fig. 1, and $\omega_{n,i}$ is the resonant angular frequency. We will call this approximation "Bessel's zero approximation" (BZA). When the radius of the cylinder is large with respect to the wavelength, one can use the asymptotic forms of the Bessel's functions to describe the radial component of the field of each mode.

$$J_n\left(\frac{\omega}{c} m_h r\right) \propto \cos\left(\frac{\omega}{c} m_h r - n\frac{\pi}{2} - \frac{\pi}{4}\right) \tag{32}$$

Under this approximation, the resonant frequencies result simply

$$\omega_{n,p} = \left(\frac{c\pi}{4 m_h R_3}\right)(2p + 2n + 1) \tag{33}$$

where p is an odd integer. We will call this Fabry-Pérot approximation as it coincide with the resonances of a Fabry-Pérot interferometer.

In Eqs. 31 and 33 we assumed the fields at the boundary of regions 2 and 3 were strictly zero and neglected the imaginary part of k_3, which

is not the case for realistic systems. To correct the formulas we propose a minimum model that only adds a constant shift $\delta\nu_{corr}$ to the lasing frequencies,

$$\nu = \frac{cu_{n,i}}{2\pi m_h R_3} + \delta\nu_{corr}. \quad (34)$$

Note, that, because of consistency, the same correction should be applied to both Eq. 31 and Eq 33. As we will see, introducing $\delta\nu_{corr}$ improves considerably the agreement with numerical results but, in exchange, now one should know *a priori* at least one lasing frequency. Despite this, one is characterizing the whole spectrum of resonant frequencies by a single parameter.

Withing the Fabry-Pérot approximation, the proportionality between ω and p causes the different modes to be equispaced in frequency. Considering the geometry studied, $m_3 \approx m_h = 1.33$ and $R_3 = 2.0\mu m$, the gap between two contiguous zeros (p and $p+2$) belonging to the same mode n is

$$\nu_{p+2} - \nu_p = 4 \times \frac{c}{(8m_h R_3)} \simeq 0.56 \times 10^{14}\text{Hz}.$$

This means that there are approximately 7 poles for each n mode within the visible spectrum, for n small. This large amount of poles shows that, given a dye, there will always be some resonance close to the maximum of its emission cross-section.

Given the sizes of the tubes used in the calculations, where the largest one has a radius of 2000 nm, and the wavelengths considered, between 400 and 800 nm, deviations respect to the Fabry-Pérot approximation are expected. We will analyze this in more details in section "Results and discussion".

Gain thresholds of cavity modes. To find an expression for the gain threshold we will use the same cavity-like model as before. We start by the gain-loss compensation condition,

$$W_{abs} = -W_{sca} \quad (35)$$

where W_{abs} and W_{sca} are the energy absorbed and scattered per unit time. The former can be calculated from

$$\begin{aligned} W_{abs} &= -\frac{c}{8\pi}\varepsilon_3'' \int_{V\in\ 3} k \left|\vec{E}\right|^2 dV \\ &\quad -\frac{c}{8\pi}\varepsilon_2'' \int_{V\in\ 2} k \left|\vec{E}\right|^2 dV \end{aligned} \quad (36)$$

where indexes 2 and 3 refers to regions 2 an 3 in Fig. 1. The energy scattered per unite time W_{sca} can be calculated from

$$\begin{aligned} W_{sca} &= \frac{c}{8\pi}\frac{4lk_0^2}{k}\sum_{n=-\infty}^{\infty} |A_{0n}|^2 \\ &\approx \frac{c}{\pi} l\varepsilon_0 k \left|A_{0n}\right|^2 \times \begin{cases} 1 & n \neq 0 \\ \frac{1}{2} & n = 0 \end{cases} \end{aligned} \quad (37)$$

where we are using the fact that, at the lasing condition, two coefficients of the summation dominate, n and $-n$. Using Eqs. 36 and 37, one can write the required condition for ε_3'' to reach the gain threshold. For $n \neq 0$ it results in

$$\varepsilon_3'' = \frac{8\varepsilon_0 - \varepsilon_2'' \int_{V\in 2} \frac{\left|\vec{E}_n\right|^2}{l|A_{0n}|^2} dV}{\int_{V\in 3} \frac{\left|\vec{E}_n\right|^2}{l|A_{0n}|^2} dV}, \quad (38)$$

where E_n is the electric field produces by the excitations of modes n and $-n$. For $n = 0$ the factor 8 should be replaced by a factor 4.

The integrals over the electric field in Eq. 38 can be written in terms of Bessel's and Hankel's functions. The result for $n \neq 0$ is

$$\int_{V\in 2}\frac{\left|\vec{E}_n\right|^2}{l\left|A_{0n}\right|^2}dV = 2\pi\int_{R_3}^{R_2}\left[\frac{|a_{2n}|^2}{|A_{0n}|^2}\left(|J_{n-1}(k_2r)|^2+|J_{n+1}(k_2r)|^2\right)\right.$$
$$+\mathrm{Re}\left\{\frac{A_{2n}a_{2n}^*}{|A_{0n}|^2}\left[H_{n-1}(k_2r)\,J_{n-1}^*(k_2r)+H_{n+1}(k_2r)\,J_{n+1}^*(k_2r)\right]\right\}$$
$$\left.+\frac{|A_{2n}|^2}{|A_{0n}|^2}\left(|H_{n-1}(k_2r)|^2+|H_{n+1}(k_2r)|^2\right)\right]|k_2|^2\,rdr \quad (39)$$

and

$$\int_{V\in 3}\frac{\left|\vec{E}_n\right|^2}{l\left|A_{0n}\right|^2}dV = 2\pi\frac{|a_{3n}|^2}{|A_{0n}|^2}\int_0^{R_3}\left(|J_{n-1}(k_3r)|^2+|J_{n+1}(k_3r)|^2\right)|k_3|^2\,rdr \quad (40)$$

where we have used the recurrent relations of J_n and H_n. For $n=0$ a 1/2 factor should be added to the right-hand side of both equations.

As we are dealing with cavity modes where the electric field is concentrated mostly within the cavity, one can assume that the integral of $|E|^2$ over region 2 in Eq. 38 is negligible. Then, Eq. 38 turns into

$$\varepsilon_3'' \approx \frac{\left(\frac{4\varepsilon_0|A_{0n}|^2}{\pi|a_{3n}|^2}\right)}{\int_0^{R_3}\left(|J_{n-1}|^2+|J_{n+1}|^2\right)|k_3|^2rdr}. \quad (41)$$

Note that the right hand side of Eqs. 38 and 41 depends on ε_3'', as the imaginary part of k_3 does. Therefore, the equation have to be solved either iteratively or by an optimization method. One approximation that can be made to avoid that, is to use the BZA discussed in the previous section, i.e. one can use Eq. 34 to estimate $k_3 \in \mathrm{Re}$. Given a value of k_3, and thus k_0, one can solve the set of linear equations given in Eqs. 8-13 to obtain the a_{jn} and A_{jn} coefficients as well as the integrals involving the Bessel's and Hankel's functions in Eq. 38 (or 41).

Despite the different approximations that one can make to estimate *a priori* the value of ε_3'', which as we will see do not work that well, Eqs. 38 and 41 can be useful for other reasons, e.g. to find the lasing conditions by directly applying an optimization method on Eqs. 38. Furthermore, the equations can also help to rationalize the observed trends in the gain threshold of different systems. For examples, according to Eq. 41, concentrating the fields on the active medium region (increasing $|a_{3n}|^2$) should reduce the gain thresholds.

RESULTS AND DISCUSSION

Using the methodology described in the previous sections, we study different geometries of multiwall micro and nanotubes. In all the figures, except in Figs. 8 and 9, we used, as a representative example, the geometry shown in Fig. 1 and discussed in section "General remarks". We first used the wideband approximation, Eq. 25, to find the poles of the system. The upper panel of Fig. 3 shows the scattering cross-section C_{sca} as a function of the imaginary part of the dielectric constant of the gain medium ε_3'' and the frequency of the incident light ν. As discussed previously, the poles of C_{sca} correspond to the full loss compensation condition, or the lasing condition. These conditions are difficult to visualize in this figure due to the large number of poles that the system present. In the lower panel of Fig. 3, we show only the position of the poles, to better visualize them.

To find the position of the poles, we used a simplex[72] algorithm to maximize the function $C_{sca}(\nu,\varepsilon'')$, starting from the maxima of C_{sca}

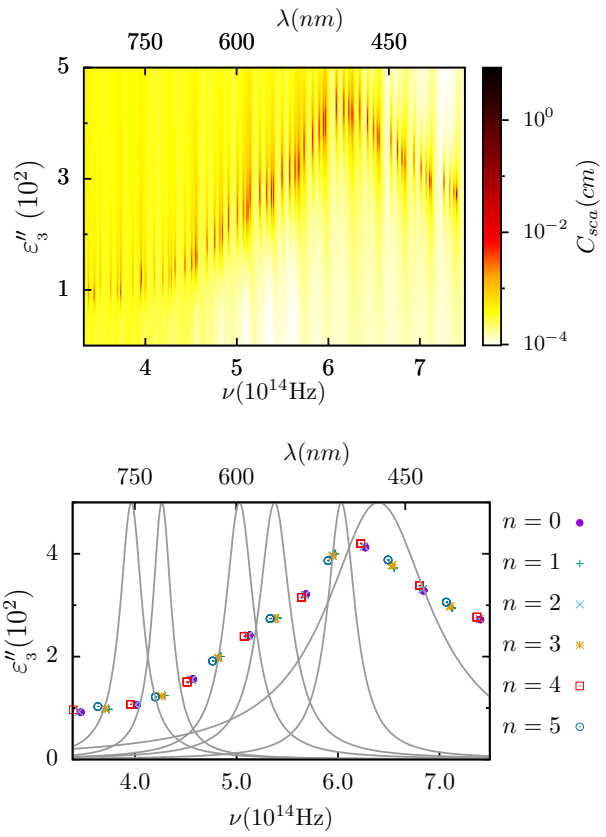

Figure 3: **Upper panel -** Scattering cross-section C_{sca} as function of the imaginary part of the dielectric constant of the gain medium ε_3'' and the frequency of the incident light ν. **Lower panel -** Position of the poles of C_{sca}, for n $(-n)$ up to 5 only, obtained within the wideband approximation. Gray lines shows the value of ε_3'' resulting from using different dyes, with $\varepsilon_l = 0.05$. From left to right, "Alexa-fluor-680", "Oregon-green-488", "Atto-rho3b", "Atto-725", "cy3b", and "tCO". See section "Parameters of the dyes".

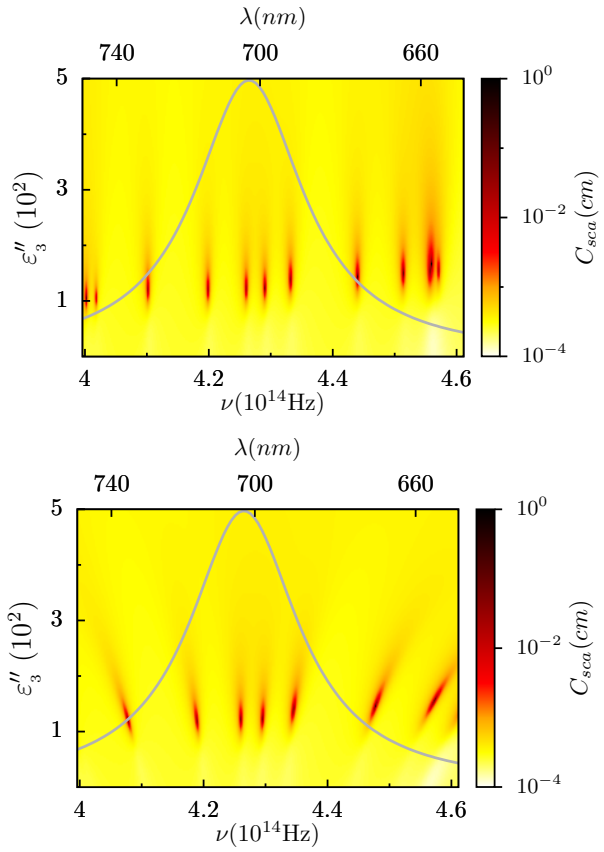

Figure 4: **Upper panel -** C_{sca} as function of ε_3'' and ν obtained using the wideband approximation, Eq. 25. **Lower panel -** The same as the upper panel but C_{sca} was calculated using Eq. 23 with Alexa-fluor-680 as the dye. The Gray lines in both figures are the values of ε_3'' obtained using Alexa-fluor-680, with $\varepsilon_l = 0.05$.

obtained from a systematic variation of ν and ε_3''. To distinguish true divergences from simple maxima, we use the fact that in a pole the iterative process will change drastically the value of C_{sca} meanwhile in a maximum the value should converge without much changes in C_{sca}. We consider a maximum as a true pole only if C_{sca} changes more than 100 times its initial value. We checked the poles found with this procedure and confirm they are in perfect agreement with Eq. 38.

The upper panel of Fig. 3 shows the enormous quantity of poles that can be achieved with relatively low gains, lower than 0.05. In the lower panel of the figure, we only show the poles up to order 5 for clarity, but in total there are around 200 poles within the visible spectrum. Superimposed on the figure, we also show the imaginary part of the dielectric constant of the active media resulting from using different dyes, see section "Parameters of the dyes". If we consider that the dyes only contribute to the imaginary part of the dielectric constant of the gain medium, all the poles below a gray curve will be reached with the dye and concentration being studied. As can be seen, it is possible to obtain TE modes of lasing all along the visible spectrum, and using moderate concentrations of the dyes, see Table 1 in section "Parameters

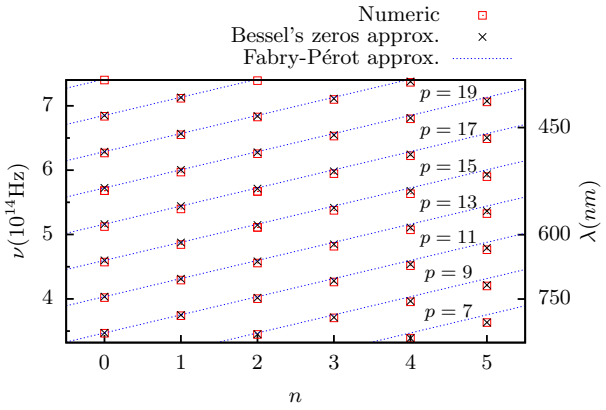

Figure 5: Comparison of the values of ν_{pole} obtained numerically, with the BZA, Eq. 31, and the Fabry-Pérot approximation, Eq. 33. For both approximations we used a constant shift of $\delta\nu_{corr} = 0.23 \times 10^{14}$Hz. The values of p used in the Fabry-Pérot approximation are indicated just above the corresponding blue lines.

of the dyes".

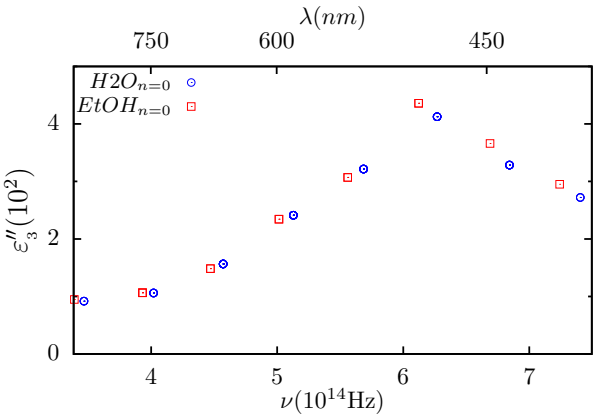

Figure 6: Example of the variation of the position of the poles induced by a change in ε_h.

It is interesting to compare the position of the poles of C_{sca} obtained with the wideband approximation with that obtained with the explicit consideration of a particular dye, using Eq. 23. This is done in Fig. 4. As expected, when the resonant frequency of a pole ν_{pole} is close to the maximum of the emission cross-section of the dye, the results for both approximations coincide. However, even when ν_{pole} is quite far from the maximum, the wideband approximation seems to work pretty well especially at predicting the values of ε''_{pole}. Only small deviations in the values of ν_{pole} were observed in such cases. This is reasonable once one realizes that, due to the low concentration of the dyes, the real part of the dielectric constant is basically that of the host medium $\mathrm{Re}\,(\varepsilon) \approx \varepsilon_h$, while its imaginary part is small, around 3% of $|\varepsilon|$.

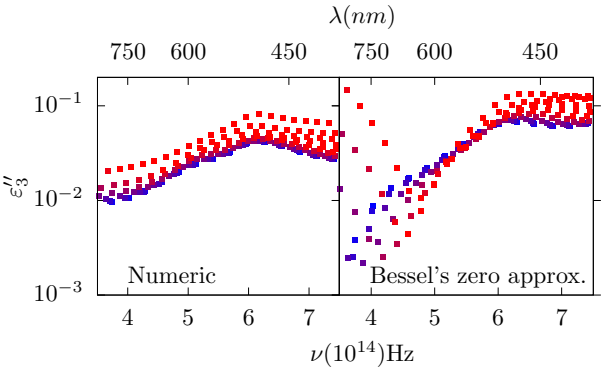

Figure 7: **Left panel -** Position of the poles of C_{sca} for all n $(-n)$ obtained numerically. **Right panel -** The same, but poles are obtained using the Bessel's zeros approximation, i.e. ν is calculated from Eq. 34 ($\delta\nu_{corr} = 0.23 \times 10^{14}$Hz) and ε''_3 is calculated from Eq. 41 with $k_3 \in$ Re estimated from Eq. 34. The color of the dots stands for the order n, low n are plotted in blue and high n in red.

Fig. 5 compares the position of the poles obtained numerically, maximizing $C_{sca}(\nu, \varepsilon'')$, with the positions predicted by the BZA, Eq. 31, and the Fabry-Pérot approximation, Eq. 33. As can be seen, the agreement with the BZA is almost perfect.

On the other hand, the agreement with the Fabry-Pérot approximation is not bad at low n. However, at higher n, the agreement worsens and modes with the same value of p significantly deviate from the predicted linear dependence with respect to n. Despite this, this simple approximation estimate, surprisingly well, the frequency separation between modes with the same n but different p, even at high values of n.

Note that in Fig. 5, only one parameter has been used to adjust both approximations, the global correction to the frequency of the poles $\delta\nu_{corr}$.

Besides its obvious application for enhanced spectroscopies, the type of system proposed can

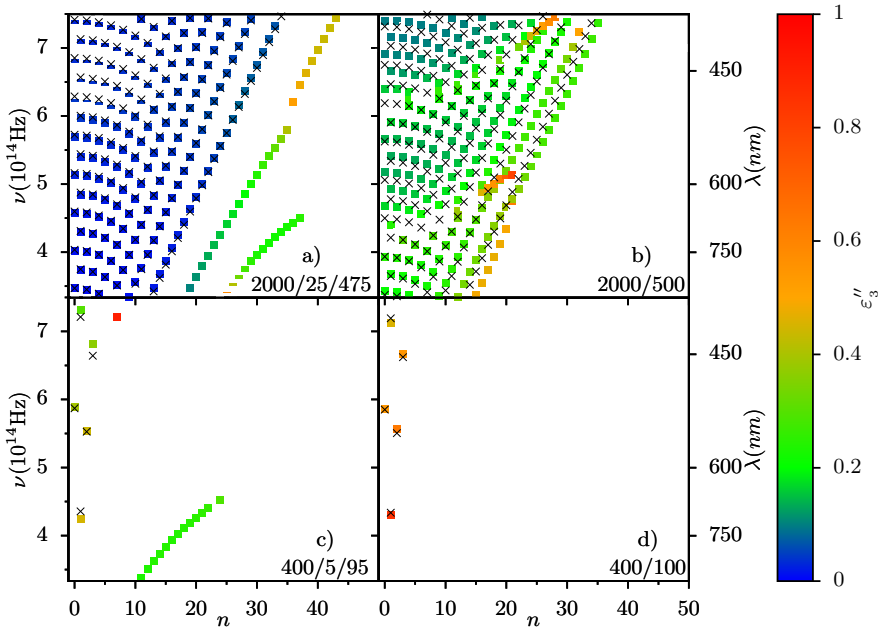

Figure 8: Filled dots corresponds to the position of the poles, ν and ε_3'', found numerically for different geometries and modes n. The crosses are the values of ν obtained using the BZA, Eq. 31. Geometries are indicated above each figure, e.g. panel (a) corresponds to $R_3 = 2000$nm, $R_2 - R_3 = 25$nm, and $R_1 - R_2 = 475$nm. The values of $\delta\nu_{corr}$ used are 0.23, 0.13, 0.92, and 0.90 (10^{14}Hz) for panels (a), (b), (c), and (d) respectively. In Fig. (a) and (c), filled dots without crosses nearby (at large n) correspond to poles of whispering-gallery modes.

be used for sensing, through changes in the dielectric constants.[36,73,74] In this case, the fact that the width of the peaks in the spectrum of micro- and nanolasers are very narrow, is a great advantage for the sensitivity of any techniques based on the shift of peaks. Fig. 6 shows the large shift of the poles with $n = 0$ caused by a slight change in the dielectric constant of the host medium ε_h, from 1.77 (water) to 1.85 (ethanol).

From the values of Fig. 6, it is possible to estimate the "refractive index sensitivity" (RIS), widely used for sensor characterization and defined as the ratio between the resonance shift $\Delta\lambda$ and the refractive index variation of the analyte, Δn.[73,74] RIS is usually measured in nm/RIU, where RIU is the abbreviation of "refractive index unit". In Fig. 6, the RIS ranges from 305 to 648 nm/RIU for $n = 0$, which is a relatively large value according to the bibliography.[73] In principle Eq. 33 could have been used to predict the variation of the position of the peaks, and the values of RIS. However, this does not lead to good estimations, since the global shift used to correct Eqs. 31 and 33, $\delta\nu_{corr}$, depends not only on the geometry of the system but also on its dielectric constants. For example, according to Eqs. 31 the change in the position of the peak at the higher frequency should be 0.23×10^{14}Hz, but the actual value is 0.162×10^{14}Hz.

Fig. 7 compares the lasing conditions obtained numerically with those found using the BZA for to the calculation of both, ν (Eq. 34 with $\delta\nu_{corr} = 0.23 \times 10^{14}$Hz) and ε_3'' (Eq. 41 with k_3 given by Eq. 34). As can be seen, the predicted values of ε_3'' deviate significantly for the lowest frequency modes where there is an unrealistic wide spread of ε_3'' values. For intermediate and high frequencies (larger than 5Hz approximately) the differences are smaller and at least the BZA estimates well the order of magnitude of ε_3''. The reason for the large errors is that both, the coefficients a_{jn} and A_{jn}, and the integrals over the Bessel and Hankel functions, are very sensitives to the exact complex value of k_3.

To compare the effect of the geometry of the

system on the lasing conditions, in Fig. 8 we show the position of the poles corresponding to four different geometries. The geometry "2000/500" is the same as "2000/25/475"(the geometry studied so far) but the gold layer has been replaced by a thicker polymer layer. The geometry "400/5/95" is the same as "2000/25/475" but rescaled by a factor 5. The same is true for the last geometry, "400/100", with respect to "2000/500". In Fig. 8, the crosses indicated the values of ν predicted by the BZA while the squares are the values of ν found numerically. In panels (a) and (c) the squares without crosses nearby correspond to WGMs. As the figure shown, the BZA is able to predict the resonant frequency ν of all the cavity modes, but only when there is a metal layer. For systems without a metal layer, see panels (b) and (d), the BZA can also work but only in limited spectral regions. As mentioned at the beginning of section "Lasing conditions", the WGMs have much higher gain thresholds than those of cavity modes for the main geometry studied, see panel (a) of Fig 8. However, for smaller systems, the increase of the gain thresholds of cavity modes makes them comparable. This is better appreciated in the upper panel of Fig. 9 where one can check that the values of ε_3'' of cavity modes and WGMs are comparable for the geometry 400/5/95.

Figs. 8 can also be used to analyze the effects of different geometries on the gain threshold of cavity modes. Broadly speaking, the figure shows that the gold layer reduces the gain thresholds, while reducing the size of the system increases the gain thresholds. This is better appreciated in Fig. 9 where we plot ε_3'' as function of $|A_{0n}|^2/|a_{3n}|^2$, which can be taken as an indicator of the confinement of the fields. Although a rigorous comparison of gain thresholds is difficult for different geometries, since the resonant frequency of the same modes changes with the geometry, the general trend for cavity modes (CM in the figure) is "the more confined the field, the lower the gain threshold" or, to be more precise, smaller values of $|A_{0n}|^2/|a_{3n}|^2$ are correlated with smaller values of ε_3''. This is in agreement with the expected trend of Eq. 41, although the lack of a proportionality relation indicates that the numerator of Eq. 41 varies significantly with the mode and the geometry of the system, or that the power dissipated by the gold layer is not completely negligible. By inspection of our results, we concluded that both contributions are responsible for the deviations. For WGM, it does not seem to be a correlation between $|A_{0n}|^2/|a_{3n}|^2$ and ε_3'', see upper panel of Fig. 9, which is natural considering that the power dissipated by the gold layer plays a central role in determining the gain thresholds in this case.

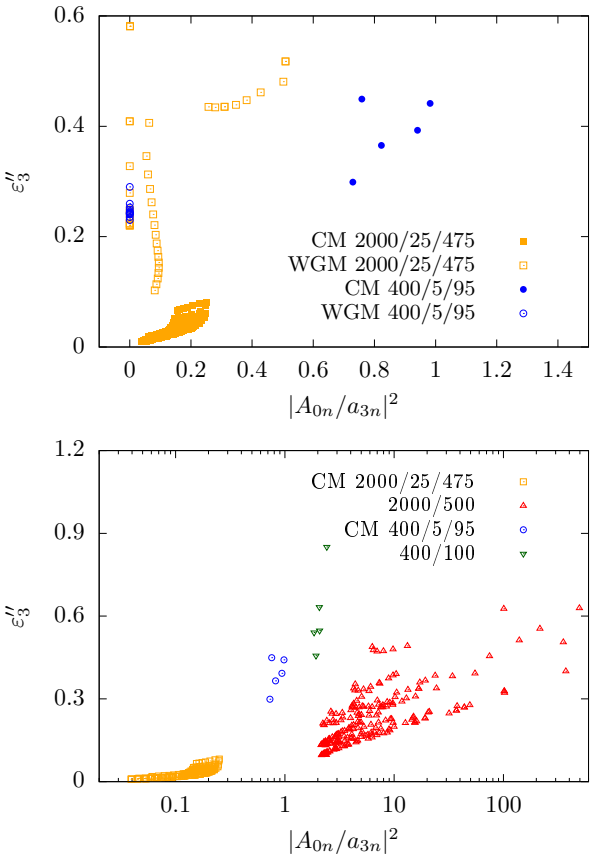

Figure 9: The imaginary part of the dielectric constant of the active medium, ε_3'', as a function of the confinement, calculated as $|A_{0n}|^2/|a_{03}|^2$, for different geometries and type of modes, indicated in the insets.

CONCLUSIONS

The studied geometry presents two types of TE modes: cavity modes and whispering-gallery-modes. Within the visible spectrum, there are

a large number of both. Cavity modes present very low gain thresholds (ε_3'' around 10^{-2}) while the WGMs exhibit gain thresholds an order of magnitude higher. The small separation between consecutive cavity modes and their much smaller gain thresholds makes WGMs hard to use for lasing. The reason for that is that the finite width of the emission cross-section of the active medium will make the population inversion of the active medium will be depleted by some cavity mode way before the lasing conditions of a WGM is reached.[67] Therefore, for the type of systems studied here, only in tubes with radii in the nanoscale, the WGMs may be used for lasing.

The very low gain thresholds of cavity modes imply that the required concentration of the dyes can be as low as $10^{-6}M$. On the other hand, the geometry studied allow one the recycling of the active medium and thus can be used to counteract the effects of photobleaching, an effect that may limit the practical applications of other proposals such as active core-shell-nanoparticles.

In the geometry studied, the frequencies of lasing can always be tunned by changing the geometry of the system but also by changing the dielectric constant of the gain medium, using different solvents for example. The latter can also be useful for sensing purposes. On the other hand, giving that the system posses so many tunable resonances, it should not be difficult, in principle, to tune a system where the maximum of the absorption cross-section of the dye and the frequency of the pump laser coincide with one resonance, while the maximum of the emission cross-section of the dye coincides with another one. This should greatly enhance the performance of the devices.

We have proposed a simple model that can accurately predict the wideband limit of the frequencies of lasing for the geometry studied. This may result especially useful in the design of the devices. On the other hand, we have shown that the deviations from the wideband approximation are not so important even for modes whose frequencies do not coincide with the maximum of the emission cross-section of the dyes.

Comparing different geometries, we have found that increasing the size of the systems, considerably reduces the gain threshold as well as increases the number of lasing frequencies within a given frequency interval. We have also shown that adding even a very small layer of a plasmonic material such a gold (a $25nm$ layer in a microtube whose total radius is $2.5\mu m$) dramatically reduces the gain threshold of the nanolaser (up to one order of magnitude). The effect of the geometry on the gain thresholds can be rationalized, at least qualitatively, in terms of the confinement of electromagnetic fields into the region of the active media.

Contrary to the longitudinal modes of lasing, which only emits plane waves, the electromagnetic fields emitted by the TE modes present hotspots without requiring additional nanostructures. Those hot spots are relatively large and can easily accommodate large macromolecules or even greater analytes such as entire cells. Moreover, the electromagnetic fields can be further enhanced with the aid of adsorbed nanoparticles, if required. In micro- and nanolasers, longitudinal modes can in principle interfere with the TE modes since they compete for the excited states to produce stimulated emission of radiation. However, their gain threshold can be independently changed by controlling their confinement, e.g. by leaving or not the tubes opened at the ends or using absorbing materials there. A possible future research direction is to compare, for the same system, the lasing conditions of longitudinal and transverse modes, addressing explicitly the problem of competition for the excited states.

In this work, we used the divergences of the scattering cross-section to find the spasing conditions, but it would be computationally useful to compare this strategy with other methods, e.g. using point-dipole emitters to look for divergences of near fields, or directly solving iteratively Eq. 38, which just express compensation of gains and losses. Moreover, for theoretical completeness, it is important to study the scattering of multiwall nanotubes for oblique illumination.

Although the system studied seems promising for several applications such as sensing or as

part of a "lab-on-chip" device, more studies are required to evaluate, for example, the intensity of the electromagnetic fields attainable for the proposed geometry, or the true potential of the system for sensing purposes.

Ultimately it would be important to experimentally test the studied geometry to contrast the theoretical results and, more importantly, the performance of the microfluidic-based recycling of the active medium.

ACKNOWLEDGEMENTS

This work was supported by Consejo Nacional de Investigaciones Científicas y Técnicas (CONICET), Argentina; Secretaría de Ciencia y Tecnología de la Universidad Nacional de Córdoba (SECYT-UNC), Córdoba, Argentina; and Universidad de Buenos Aires, Project UBA 20020100100327, Buenos Aires, Argentina.

References

(1) Ma, R.-M.; Oulton, R. F. Whispering-gallery mode microdisk lasers. *Appl. Phys. Lett.* **1992**, *60*, 289–291.

(2) Painter, O. e. a. Two-dimensional photonic band-gap defect mode laser. *Science* **1999**, *284*, 1819–1821.

(3) Johnson, J. C. e. a. Single nanowire lasers. *J. Phys. Chem. B* **2001**, *105*, 11387–11390.

(4) Deeb, C.; Pelouard, J.-L. Plasmon lasers: coherent nanoscopic light sources. *Phys. Chem. Chem. Phys.* **2017**, *19*, 29731–29741.

(5) Bergman, D. J.; Stockman, M. I. Surface Plasmon Amplification by Stimulated Emission of Radiation: Quantum Generation of Coherent Surface Plasmons in Nanosystems. *Phys. Rev. Lett.* **2003**, *90*, 027402.

(6) Wang, D.; Wang,; Weijia,; Knudson,; P, M.; Schatz,; C, G.; Odom,; W, T. Structural engineering in plasmon nanolasers. *Chem. Rev.* **2017**, *118*, 2865–2881.

(7) Berini, P.; De Leon, I. Surface plasmon–polariton amplifiers and lasers. *Nat. Photon.* **2012**, *6*, 16.

(8) Hill, M. T.; Gather, M. C. Advances in small lasers. *Nat. Photon.* **2014**, *8*, 908.

(9) Törmä, P.; Barnes, W. L. Strong coupling between surface plasmon polaritons and emitters: a review. *Rep. Prog. Phys.* **2015**, *78*, 013901.

(10) Amendola, V.; Pilot, R.; Frasconi, M.; Marago, O. M.; Iati, M. A. Surface plasmon resonance in gold nanoparticles: a review. *J. Phys. Condens. Matter* **2017**, *29*, 203002.

(11) Ma, R.-M.; Oulton, R. F. Applications of nanolasers. *Nat. Nanotech.* **2018**, *14*, 12.

(12) Liu, B.; Zhu, W.; Gunapala, S. D.; Stockman, M. I.; Premaratne, M. Open resonator electric spaser. *ACS nano* **2017**, *11*, 12573–12582.

(13) Warnakula, T.; Stockman, M. I.; Premaratne, M. Improved scheme for modeling a spaser made of identical gain elements. *J. Opt. Soc. Am. B* **2018**, *35*, 1397–1407.

(14) Huang, Y.; Bian, X.; Ni, Y. X.; Miroshnichenko, A. E.; Gao, L. Nonlocal surface plasmon amplification by stimulated emission of radiation. *Phys. Rev. A* **2014**, *89*, 053824.

(15) Parfenyev, V. M.; Vergeles, S. S. Quantum theory of a spaser-based nanolaser. *Opt. Express* **2014**, *22*, 13671–13679.

(16) Hapuarachchi, H.; Gunapala, S. D.; Bao, Q.; Stockman, M. I.; Premaratne, M. Exciton behavior under the influence of metal nanoparticle near fields: Significance of nonlocal effects. *Phys. Rev. B* **2018**, *98*, 115430.

(17) Zhong, X.-L.; Li, Z.-Y. All-analytical semiclassical theory of spaser performance in a plasmonic nanocavity. *Phys. Rev. B* **2013**, *88*, 085101.

(18) Ambati, M.; Nam, S. H.; Ulin-Avila, E.; Genov, D. A.; Bartal, G.; Zhang, X. Observation of Stimulated Emission of Surface Plasmon Polaritons. *Nano Lett.* **2008**, *8*, 3998–4001.

(19) Noginov, M.; Zhu, G.; Belgrave, A.; Bakker, R.; Shalaev, V.; Narimanov, E.; Stout, S.; Herz, E.; Suteewong, T.; Wiesner, U. Demonstration of a spaser-based nanolaser. *Nature* **2009**, *460*, 1110.

(20) Ma, R.-M.; Ota, S.; Li, Y.; Yang, S.; Zhang, X. Explosives detection in a lasing plasmon nanocavity. *Nat. Nanotechnol.* **2014**, *9*, 600.

(21) Kiraz, A.; Chen, Q.; Fan, X. Optofluidic lasers with aqueous quantum dots. *ACS photonics* **2015**, *2*, 707–713.

(22) Lai, C.-C.; Ke, C.-P.; Tsai, C.-N.; Lo, C.-Y.; Shr, R.-C.; Chen, M.-H. Near-field lasing dynamics of a crystal-glass core–shell hybrid fiber. *J. Phys. Chem. C* **2013**, *117*, 17725–17730.

(23) Chandrahalim, H.; Chen, Q.; Said, A. A.; Dugan, M.; Fan, X. Monolithic optofluidic ring resonator lasers created by femtosecond laser nanofabrication. *Lab on a Chip* **2015**, *15*, 2335–2340.

(24) Zapf, M.; Röder, R.; Winkler, K.; Kaden, L.; Greil, J.; Wille, M.; Grundmann, M.; Schmidt-Grund, R.; Lugstein, A.; Ronning, C. Dynamical Tuning of Nanowire Lasing Spectra. *Nano lett.* **2017**, *17*, 6637–6643.

(25) Lin, J.-D.; Lin, H.-Y.; Wei, G.-J.; Chuang, Y.-C.; Lin, L.-J.; Mo, T.-S.; Lee, C.-R. Broadband-tunable photonic bandgap and thermally convertible laser with ultra-low lasing threshold in a refilled chiral polymer template. *J. Mater. Chem. C* **2019**, Advance Article.

(26) Chua, S.-L.; Zhen, B.; Lee, J.; Bravo-Abad, J.; Shapira, O.; Soljačić, M. Modeling of threshold and dynamics behavior of organic nanostructured lasers. *J. Mater. Chem. C* **2014**, *2*, 1463–1473.

(27) Zhao, F.; Zeng, J.; Arnob, M. M. P.; Sun, P.; Qi, J.; Motwani, P.; Gheewala, M.; Li, C.-H.; Paterson, A.; Strych, U. et al. Monolithic NPG nanoparticles with large surface area, tunable plasmonics, and high-density internal hotspots. *Nanoscale* **2014**, *6*, 8199–8207.

(28) Li, Q.; Liu, Y.; Chen, P.; Hou, J.; Sun, Y.; Zhao, G.; Zhang, N.; Zou, J.; Xu, J.; Fang, Y. et al. Excitonic Luminescence Engineering in Tervalent-Europium-Doped Cesium Lead Halide Perovskite Nanocrystals and Their Temperature-Dependent Energy Transfer Emission Properties. *J. Phys. Chem. C* **2018**, *122*, 29044–29050.

(29) Shah, G. A. Scattering of Plane Electromagnetic Waves by Infinite Concentric Circular Cylinders at Oblique Incidence. *Mon. Notices Royal Astron. Soc.* **1970**, *148*, 93.

(30) Kerker, M.; E. Matijević, E. Scattering of Electromagnetic Waves from Concentric Infinite Cylinders. *J. Opt. Soc. Am.* **1961**, *51*, 506–508.

(31) van de Hulst, H. C. *Light Scattering by Small Particles*; Dover Publications Inc, Mineola, New York, USA, 1981.

(32) Bohren, C. F.; Huffman, D. R. *Absorption and scattering of light by small particles*; Wiley Interscience, New York, USA, 2008.

(33) Yarin, A. L.; Zussman, E.; Wendorff, J.; Greiner, A. Material encapsulation and transport in core–shell micro/nanofibers, polymer and carbon nanotubes and micro/nanochannels. *J. Mater. Chem.* **2007**, *17*, 2585–2599.

(34) Dror, Y.; Salalha, W.; Avrahami, R.; Zussman, E.; Yarin, A.; Dersch, R.;

Greiner, A.; Wendorff, J. One-step production of polymeric microtubes by co-electrospinning. *small* **2007**, *3*, 1064–1073.

(35) VanDersarl, J. J.; Xu, A. M.; Melosh, N. A. Nanostraws for direct fluidic intracellular access. *Nano lett.* **2011**, *12*, 3881–3886.

(36) Kim, K. H.; Bahl, G.; Lee, W.; Liu, J.; Tomes, M.; Fan, X.; Carmon, T. Cavity optomechanics on a microfluidic resonator with water and viscous liquids. *Light Sci. Appl.* **2013**, *2*, e110.

(37) Hu, J.; Li, W.; Chen, J.; Zhang, X.; Zhao, X. Novel plating solution for electroless deposition of gold film onto glass surface. *Surf. Coat. Technol.* **2008**, *202*, 2922–2926.

(38) Formanek, F.; Takeyasu, N.; Tanaka, T.; Chiyoda, K.; Ishikawa, A.; Kawata, S. Selective electroless plating to fabricate complex three-dimensional metallic micro/nanostructures. *Appl. Phys. Lett.* **2006**, *88*, 083110.

(39) Demoustier-Champagne, S.; Delvaux, M. Preparation of polymeric and metallic nanostructures using a template-based deposition method. *Mater. Sci. Eng., C* **2001**, *15*, 269–271.

(40) Garreau, A.; Duvail, J.-L. Recent Advances in Optically Active Polymer-Based Nanowires and Nanotubes. *Adv. Opt. Mater.* **2014**, *2*, 1122–1140.

(41) Hill, M. T. e. a. Lasing in metallic-coated nanocavities. *Nat. Photon.* **2007**, *1*, 589–594.

(42) Nezha, M. P. e. a. Room-temperature subwavelength metallo-dielectric lasers. *Nat. Photon.* **2010**, *4*, 395–399.

(43) Ding, K. e. a. An electrical injection metallic cavity nanolaser with azimuthal polarization. *Appl. Phys. Lett.* **2013**, *102*, 041110.

(44) Pan, A.; Liu, D.; Liu, R.; Wang, F.; Zhu, X.; Zou, B. Optical Waveguide through CdS Nanoribbons. *Small* **2005**, *1*, 980–983.

(45) Shevchenko, A.; Lindfors, K.; Buchter, S.; Kaivola, M. Evanescent-wave pumped cylindrical microcavity laser with intense output radiation. *Opt. Commun.* **2005**, *245*, 349–353.

(46) Moon, H.-J.; Park, G.-W.; Lee, S.-B.; An, K.; Lee, J.-H. Laser oscillations of resonance modes in a thin gain-doped ring-type cylindrical microcavity. *Opt. Commun.* **2004**, *235*, 401–407.

(47) Parola, I.; Illarramendi, M.; Arrue, J.; Ayesta, I.; Jiménez, F.; Zubia, J.; Tagaya, A.; Koike, Y. Characterization of the optical gain in doped polymer optical fibres. *J. Lumin.* **2016**, *177*, 1–8.

(48) Saleh, A. A.; Dionne, J. A. Waveguides with a silver lining: Low threshold gain and giant modal gain in active cylindrical and coaxial plasmonic devices. *Phys. Rev. B* **2012**, *85*, 045407.

(49) Wang, X.; Zhuang, X.; Yang, S.; Chen, Y.; Zhang, Q.; Zhu, X.; Zhou, H.; Guo, P.; Liang, J.; Huang, Y. et al. High Gain Submicrometer Optical Amplifier at Near-Infrared Communication Band. *Phys. Rev. Lett.* **2015**, *115*, 027403.

(50) Wang, X.; Shoaib, M.; Wang, X.; Zhang, X.; He, M.; Luo, Z.; Zheng, W.; Li, H.; Yang, T.; Zhu, X. et al. High-Quality In-Plane Aligned CsPbX3 Perovskite Nanowire Lasers with Composition-Dependent Strong Exciton–Photon Coupling. *ACS Nano* **2018**, *12*, 6170–6178.

(51) Bordo, V. Model of Fabry-Pérot-type electromagnetic modes of a cylindrical nanowire. *Phys. Rev. B* **2010**, *81*, 035420.

(52) Tong, L.; Lou, J.; Mazur, E. Single-mode guiding properties of subwavelength-

diameter silica and silicon wire waveguides. *Opt. Express* **2004**, *12*, 1025–1035.

(53) Huang, D.; Li, T.; Liu, S.; Yi, T.; Wang, C.; Li, J.; Liu, X.; Xu, M. Random lasing action from electrospun nanofibers doped with laser dyes. *Laser Phys.* **2017**, *27*, 035802.

(54) Persano, L.; Camposeo, A.; Pisignano, D. Active polymer nanofibers for photonics, electronics, energy generation and micromechanics. *Prog. Polym. Sci.* **2015**, *43*, 48–95.

(55) Gu, F.; Yu, H.; Wang, P.; Yang, Z.; Tong, L. Light-emitting polymer single nanofibers via waveguiding excitation. *ACS nano* **2010**, *4*, 5332–5338.

(56) Camposeo, A.; Di Benedetto, F.; Stabile, R.; Neves, A. A.; Cingolani, R.; Pisignano, D. Laser emission from electrospun polymer nanofibers. *Small* **2009**, *5*, 562–566.

(57) Ishii, Y.; Satozono, S.; Omori, K.; Fukuda, M. Waveguiding properties in dye-doped submicron poly (N–vinylcarbazole) fibers. *J. Polym. Sci. B* **2016**, *54*, 1237–1244.

(58) Tang, S. K.; Li, Z.; Abate, A. R.; Agresti, J. J.; Weitz, D. A.; Psaltis, D.; Whitesides, G. M. A multi-color fast-switching microfluidic droplet dye laser. *Lab Chip* **2009**, *9*, 2767–2771.

(59) Vasdekis, A.; Town, G.; Turnbull, G.; Samuel, I. Fluidic fibre dye lasers. *Opt. Express* **2007**, *15*, 3962–3967.

(60) Goldberger, J.; Fan, R.; Yang, P. Inorganic nanotubes: a novel platform for nanofluidics. *Acc. Chem. Res* **2006**, *39*, 239–248.

(61) Wirtz, M.; Yu, S.; Martin, C. R. Template synthesized gold nanotube membranes for chemical separations and sensing. *Analyst* **2002**, *127*, 871–879.

(62) Wirtz, M.; Martin, C. R. Template-fabricated gold nanowires and nanotubes. *Adv. Mater.* **2003**, *15*, 455–458.

(63) Johnson, P. B.; Christy, R.-W. Optical constants of the noble metals. *Phys. Rev. B* **1972**, *6*, 4370.

(64) Sultanova, N.; Kasarova, S.; Nikolov, I. Dispersion Properties of Optical Polymers. *Acta Phys. Pol. A* **2009**, *116*, 585–587.

(65) Gurwich, I.; Shiloah, N.; Kleiman, M. The recursive algorithm for electromagnetic scattering by tilted infinite circular multilayered cylinder. *J. Quant. Spectrosc. Radiat. Transf.* **1999**, *63*, 217–229.

(66) Dattoli, G.; Torre, A. *Theory and applications of generalized Bessel functions*; ARACNE, Rome, Italy, 1996.

(67) Passarelli, N.; Bustos-Marún, R. A.; Coronado, E. A. Spaser and optical amplification conditions in gold-coated active nanoparticles. *J. Phys. Chem. C* **2016**, *120*, 24941–24949.

(68) Novotny, L.; Hecht, B. *Principles of nano-optics*; Cambridge university press, New York, USA, 2012.

(69) Arnold, N.; Piglmayer, K.; Kildishev, A. V.; Klar, T. A. Spasers with retardation and gain saturation: electrodynamic description of fields and optical cross-sections. *Opt. Mater. Express* **2015**, *5*, 2546–2577.

(70) Pollnau, M.; Eichhorn, M. In *Nano-Optics: Principles Enabling Basic Research and Applications. NATO Science for Peace and Security Series B: Physics and Biophysics*; Di Bartolo, B., Collins, J., Silvestri, L., Eds.; Springer, Dordrecht, The Netherlands, 2017; Chapter 19, pp 387–404.

(71) *The Fluorophores.org database.*; Initiated by the Applied Sensor Group of the Institute of Analytical Chemistry at the

Graz University of Technology in Austria. http://www.fluorophores.tugraz.at/.

(72) Press, W. H.; Teukolsky, S. A.; Vetterling, W. T.; Flannery, B. P. *Numerical Recipes in FORTRAN 77. The Art of Scientific Computing.*, 2nd ed.; Cambridge University Press, New York, USA, 1995.

(73) Kedem, O.; Vaskevich, A.; Rubinstein, I. Critical Issues in Localized Plasmon Sensing. *J. Phys. Chem. C* **2014**, *118*, 8227–8244.

(74) Špačková, P.; Wrobel,; Bocková, M.; Homola, J. Optical biosensors based on plasmonic nanostructures: a review. *Proc. IEEE* **2016**, *23*, 2380–2408.

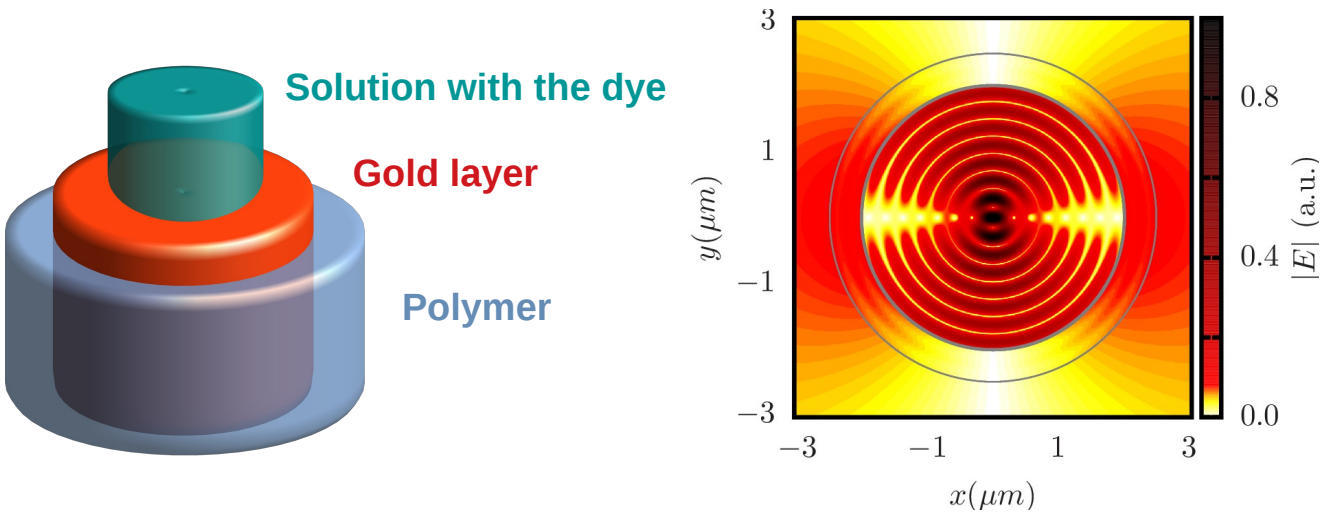

Figure 10: **TOC graphic.**